# Electrocatalytic Nitrate Reduction on Oxide-Derived Silver with Tunable Selectivity to Nitrite and Ammonia

Hengzhou Liu, Jaeryul Park, Yifu Chen, Yang Qiu, Yan Cheng, Kartik Srivastava, Shuang Gu, Brent H. Shanks, Luke T. Roling,* Wenzhen Li*

**ABSTRACT:** *Removing excess nitrate ($NO_3^-$) from waste streams has become a significant environmental and health topic. However, realizing highly selective $NO_3^-$ conversion towards $N_2$, primarily via electrocatalytic conversions, has proven challenging, largely because of the kinetically uncontrollable $NO_3^-$-to-$NO_2^-$ pathway and unfavorable N-N coupling. Herein, we discovered unique and ultra-high electrocatalytic $NO_3^-$-to-$NO_2^-$activity on oxide-derived silver (OD-Ag). Up to 98% selectivity and 95% faradaic efficiency of $NO_2^-$ were observed and maintained under a wide potential window. Benefiting from the superior $NO_3^-$-to-$NO_2^-$activity, further reduction of accumulated $NO_2^-$ to $NH_4^+$ was well regulated by the cathodic potential and achieved an $NH_4^+$ faradaic efficiency of 89%, indicating a tunable selectivity to the key nitrate reduction products ($NO_2^-$or $NH_4^+$) on OD-Ag. DFT computations provided insights into the unique $NO_2^-$selectivity on Ag electrodes compared with Cu, showing the critical role of a proton-assisted mechanism. Based on the ultra-high $NO_3^-$-to-$NO_2^-$activity on OD-Ag, we designed a novel electrocatalytic-catalytic combined process for denitrifying real-world $NO_3^-$-containing agricultural wastewater, leading to 95+% of $NO_3^-$ conversion to $N_2$ with minimal $NO_X$ gases. In addition to the wastewater treatment process to $N_2$ and electrochemical synthesis of $NH_3$, $NO_2^-$ derived from electrocatalytic $NO_3^-$ conversion can serve as a reactive platform for distributed production of various nitrogen products.*

**KEYWORDS:** *Density Functional Theory · Electrocatalysis · Heterogeneous Catalysis · Nitrate Reduction · Selectivity · Wastewater Treatment*

## INTRODUCTION

Nitrate ($NO_3^-$) is a toxic chemical increasingly found in agricultural runoff and industrial wastes. Nitrate is directly responsible for the notorious eutrophication in natural waters as well as other environmental problems.[1] The waste nitrate also finds its way to drinking water, and the intake of excess nitrate has been linked to severe health issues,[2] specific cancers, and birth defects.[3] A recent study showed that the existing nitrate pollution of U.S. drinking water might cause more than 12,500 cases of cancer each year,[4] and wastewater treatment accounts for about 3–4% of the U.S.'s electrical energy load.[5]

Currently, $NO_3^-$ can be removed by biological denitrification,[6-7] reverse osmosis,[8] and ion exchange.[9] The biological approach is inexpensive; however, the growth of bacteria requires additional purification. Both reverse osmosis and ion exchange are useful. However, the created concentrated nitrate-containing wastes, required harsh reaction conditions (e.g., high pressure, specific pH, $H_2$ feeding), and exhibited relatively low sensitivity toward $NO_3^-$ ion largely increased the energy and materials cost as well as induced additional pre-treatment and post-disposal processes.

Alternatively, electrocatalytic reduction reactions can be driven by renewable electricity from wind and sunlight, substituted expensive $H_2$ by water, and operated under mild conditions, which offers an opportunity to convert $NO_3^-$ to $N_2$ for closing the loop of the global N cycle.[10-11] However, achieving high selectivity towards the desirable $N_2$ has proven kinetically challenging,[12] especially via electrochemical conversions, in part because the N-N coupling reaction is rather difficult and competes with the facile kinetics to $NH_4^+$/$NH_3$ and $H_2$ (from hydrogen evolution reaction (HER)).[13-15] In particular, the $NO_3^-$-to-$NO_2^-$ reaction, which regulated the $NO_3^-$ reduction pathway and typically controlled the overall rate towards different N-species, was confirmed challenging to be well-manipulated.[16-17] Additionally, most report electrochemically produced $N_2$ (<30% selectivity) was based on nitrogen balance estimation (produced $N_2$ = reacted $NO_3^-$ – produced $NO_2^-$ and $NH_4^+$).[12,13] This indirectly quantified $N_2$ failed to rule out the following possibilities: (1) experimental errors in the quantification of $NO_3^-$, $NO_2^-$, and $NH_4^+$, (2) possible $NO_x$ (NO, $NO_2$, and $N_2O$) intermediates, (3) imperfectly sealed reactors during sample collection and transformation, as 79% $N_2$ in the air may largely interfere with accurate $N_2$ quantification. Hence, establishing accurate nitrogen and electron balance is necessary but still challenging for the N-cycle chemistry management, especially considering a series of possible N-containing

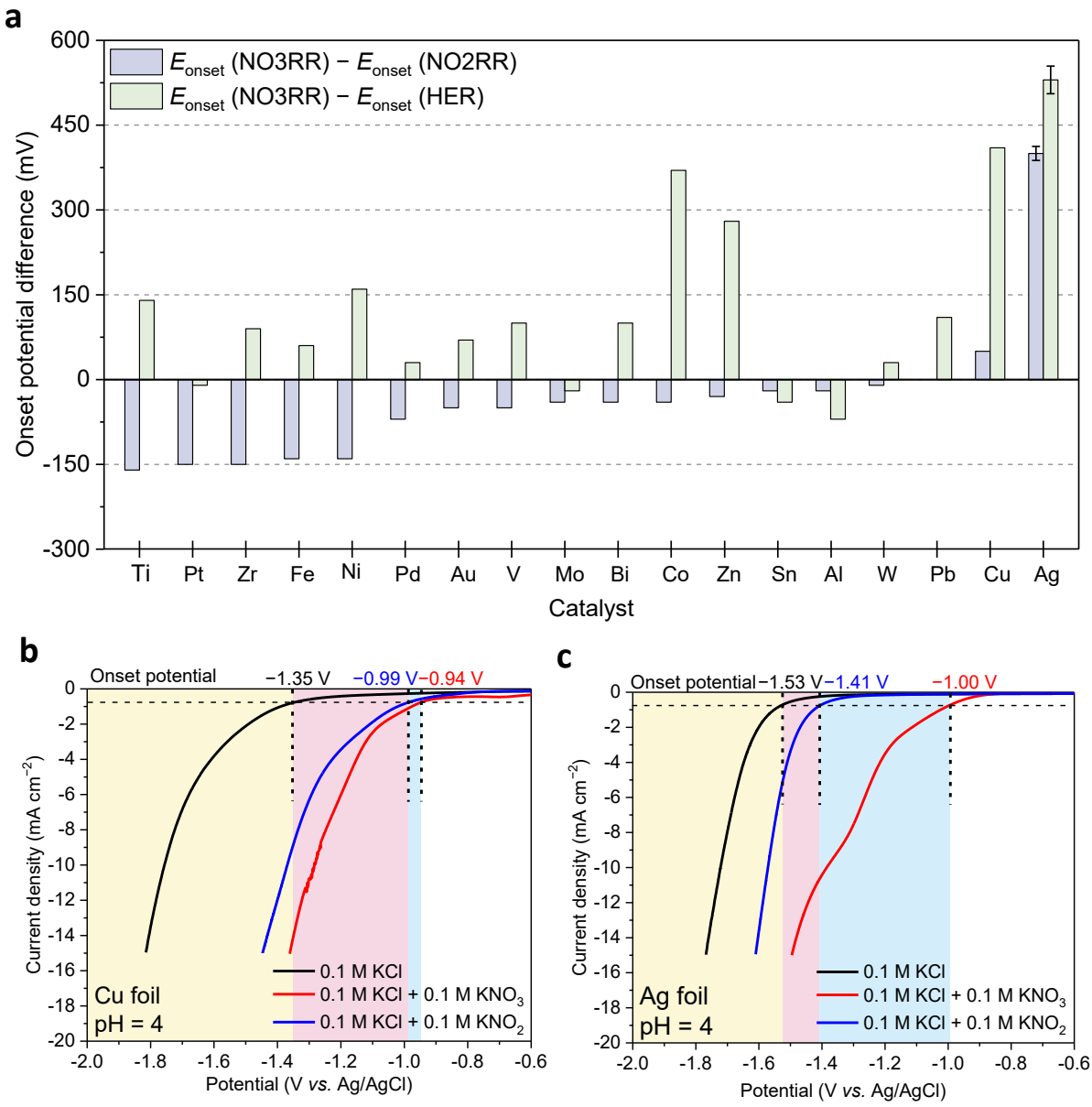


**Figure 1.** Metal surfaces with a distinctive electrocatalytic preference between $NO_3^-$ reduction and $NO_2^-$ reduction. (a) The onset-potential difference between $NO_3^-$ reduction and $NO_2^-$ reduction: "$E_{onset}$(NO3RR) − $E_{onset}$(NO2RR)", and the onset-potential difference between $NO_3^-$ reduction and HER: "$E_{onset}$(NO3RR) − $E_{onset}$(HER)". The detailed LSV curves to obtain onset potentials are shown in Figure S1a–p. The error bars represent the standard deviation from at least three independent measurements. (b)–(c) LSV curves on Cu foil and Ag foil in three different solutions: 0.1 M KCl (black curve), 0.1 M KCl with 0.1 M $NO_3^-$ (red curve), and 0.1 M KCl with 0.1 M $NO_2^-$ (blue curve). A scan rate of 5 mV $s^{-1}$ was the same for LSV on all metal surfaces, and all electrolytes were adjusted to pH 4. The geometric area of all metal foils was 4 $cm^2$.

intermediates exist from the highest valance of N in $NO_3^-$ to the lowest of N in $NH_4^+$ (e.g., $NO_2$, $NO_2^-$, NO, $N_2O$, $N_2$, $NH_2OH$, $NH_4^+$, etc.).

In addition to converting fixed N (e.g., $NO_3^-$ or $NO_2^-$) to inert $N_2$ for denitrifying wastewater, recent studies have highlighted that electrochemical transformation of $NO_3^-$ to $NH_4^+$ (in particular from nitrate-rich waste streams) holds promise to mitigate the need for $NH_3$ production from the energy-intensive Haber-Bosch process.[18-20] Electrochemical ammonia synthesis, particularly from $NO_3^-$ conversion, not only helps address the environmental problem, but also holds the potential to reduce energy consumption, as ammonia is an irreplaceable fertilizer and essential precursor for fuels and chemicals.[21] Therefore, it is critical to acquire a deep understanding of nitrate reduction mechanisms and rationally design electrocatalysts or processes to carefully manipulate $NO_3^-$ reduction pathways towards desired products.

Herein, we discovered the unique selectivity and superior activity on OD-Ag electrocatalyst for converting $NO_3^-$ to $NO_2^-$. Up to 98% selectivity and 95% faradaic efficiency (FE) of $NO_2^-$ were achieved and well-maintained

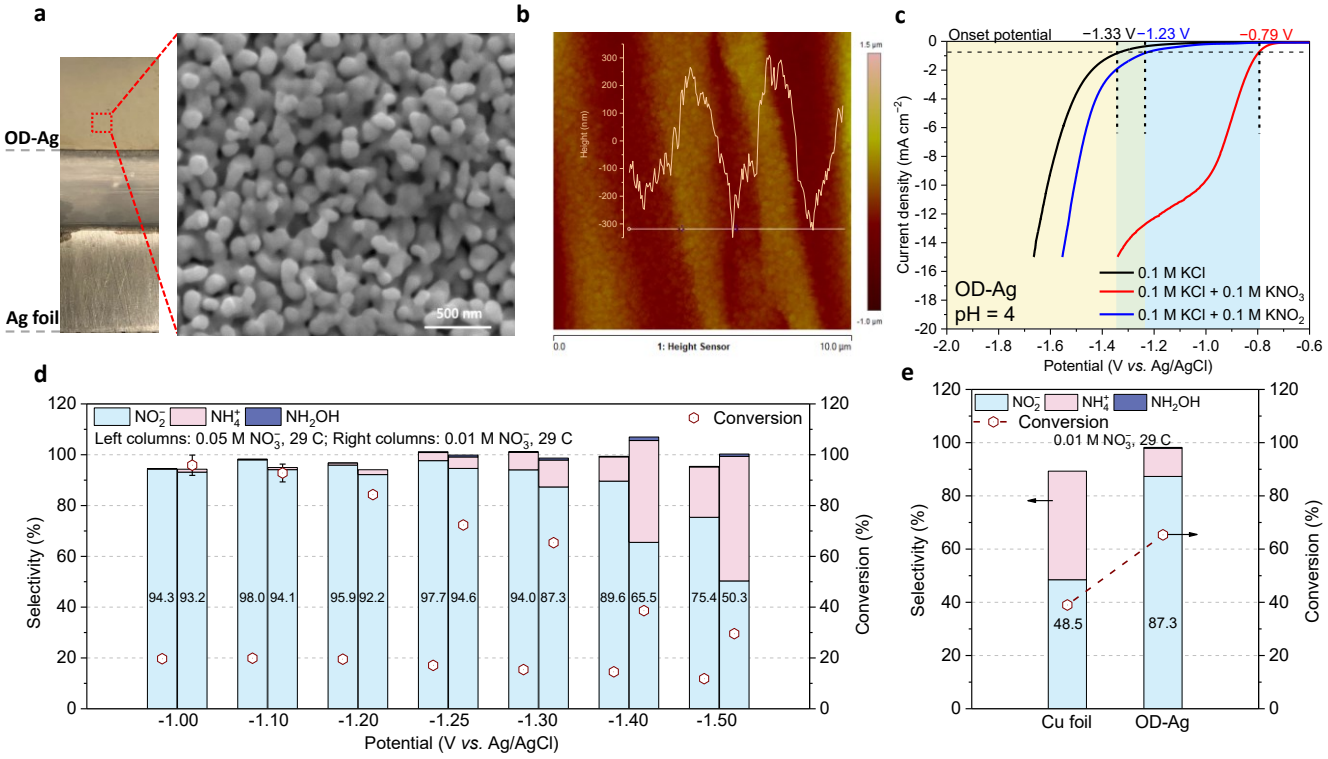


**Figure 2**. NO3RR performance on OD-Ag at pH 4. (a) Photograph and SEM image of OD-Ag. (b) AFM image of OD-Ag. The inset graph is the height profile of a 7-μm section (the white line). (c) Linear sweep voltammetry of OD-Ag in three different solutions: 0.1 M KCl (black curve), 0.1 M KCl with 0.1 M $NO_3^-$ (red curve), and 0.1 M KCl with 0.1 M $NO_2^-$ (blue curve). The onset potentials for NO3RR, NO2RR, and HER are marked, leading to the "$E_{onset}$(NO3RR) − $E_{onset}$(NO2RR)" = 440 mV, and "$E_{onset}$(NO3RR) − $E_{onset}$(HER)" = 540 mV. The geometric area for OD-Ag was 4 $cm^2$. (d) Product selectivity and conversion of $NO_3^-$ in 0.1 M KCl with 0.05 M $NO_3^-$ (left columns) and 0.01 M $NO_3^-$ (right columns) at different applied potentials on OD-Ag with 29 C applied charge. The error bars represent the standard deviation for at least three independent measurements. (e) 0.01 M $NO_3^-$ at −1.30 $V_{Ag/AgCl}$ on different electrodes. The geometric area of the electrode was 6 $cm^2$ for −1.00 and −1.10 $V_{Ag/AgCl}$ with 0.01 M $NO_3^-$, and 2 $cm^2$ for all other conditions. The methods of product detection are detailed in the Supporting Information, and their calibrations are shown in Figure S5−6.

in a wide potential window. Moreover, electro-kinetics identified the selective conversion of $NO_3^-$ to $NO_2^-$ and further reduction of $NO_2^-$ to $NH_4^+$ can be well regulated by cathodic potential. Benefiting from the superior $NO_3^-$-to-$NO_2^-$ activity, 99% of $NO_3^-$ can be converted to $NH_4^+$ with a FE of 89% when the applied potential exceeds an apparent gating potential via passing the theoretical charge (116 C) from $NO_3^-$ to $NH_4^+$. DFT computations provided insights into the unique $NO_2^-$selectivity on Ag electrodes compared with Cu, showing the critical role of a proton-assisted mechanism. We further proposed a combined electrocatalytic-catalytic process by splitting the scientific challenge of electrochemical $NO_3^-$-to-$N_2$ conversion into two steps: electrocatalytic $NO_3^-$-to-$NO_2^-$ step on oxide-derived Ag (OD-Ag), with a subsequent catalytic $NO_2^-$-to-$N_2$ step on a Pd catalyst using $H_2$ generated on-site by a PEM-based water electrolyzer. The combined process ultimately removed 95+% of $NO_3^-$ from real-world agricultural wastewater to $N_2$, leaving the residual N in the treated solutions with <3.5 ppm of $NH_4^+$-N. Our entire combined process can be powered by renewable electricity and as an innovative strategy for facile converting $NO_3^-$ to $N_2$, thus opening a new scenario for the N-cycle management towards an N-neutral future.

## RESULTS AND DISCUSSION

**Strong electrocatalytic preference on Ag for $NO_3^-$ reduction over $NO_2^-$ reduction.** Owing to the higher reactivity of $NO_2^-$ than the stable $NO_3^-$, it is generally easier to electrochemically reduce $NO_2^-$ on most metal surfaces. Indeed, as observed in linear sweep voltammetry (LSV, Figure S1), 15 of 18 commonly used metal foils possessed a more negative onset potential for the $NO_3^-$ reduction reaction (NO3RR) than for the $NO_2^-$ reduction reaction (NO2RR), rendering the onset-potential difference [*i.e.*, "$E_{onset}$(NO3RR) − $E_{onset}$(NO2RR)"] negative: gradually from −160 to −10 mV on Ti, Pt, Zr, Fe, Ni, Pd, Au, V, Mo, Bi, Co, Zn, Sn, Al, and W, respectively (Figure 1a and Table S1). Note that the onset potential was consistently defined as the potential under which −0.75 mA $cm^{-2}$ was reached in LSV for NO3RR, NO2RR, and HER in this work. This selected current density represented the apparent occurrence of corresponding reactions without interference by the electrode double-layer charging-discharging. A positive onset-potential difference indicated more favorable NO3RR than NO2RR or HER. Clearly, those 15 metal surfaces prefer the NO2RR to the NO3RR under the same test conditions. No preference between NO3RR and NO2RR was observed

on Pb foil: the onset potential of the NO3RR was precisely the same as that of the NO2RR (−1.60 $V_{Ag/AgCl}$, $V_{Ag/AgCl}$: V *vs.* Ag/AgCl, hereinafter).

Interestingly, Cu and Ag are the only two metal surfaces that showed the distinctive preference for NO3RR over NO2RR: the "$E_{onset}$(NO3RR) − $E_{onset}$(NO2RR)" is positive. Specifically, the onset potentials of the NO3RR in LSV are very close to each other: −1.00 $V_{Ag/AgCl}$ and −0.94 $V_{Ag/AgCl}$ on Ag and Cu, respectively (Figure 1b–c). Importantly, the onset potential of the NO2RR is far more negative on Ag than on Cu (−1.41 $V_{Ag/AgCl}$ *vs.* −0.99 $V_{Ag/AgCl}$), substantiating the higher energy barrier of $NO_2^-$ reduction on the Ag surface. Therefore, as shown in Figure 1b–c blue region, the potential window between NO3RR and NO2RR onsets is significantly wider on Ag than on Cu (410 mV *vs.* 50 mV). In addition, Ag holds 180 mV more negative onset potential for HER than Cu (−1.53 $V_{Ag/AgCl}$ *vs.* −1.35 $V_{Ag/AgCl}$), and the "$E_{onset}$(NO3RR) − $E_{onset}$(HER)" is 530 mV (Ag) *vs.* 410 mV (Cu) (Figure 1b–c blue + orange region). The strong preference for the NO3RR over the NO2RR and HER could be particularly beneficial for selectively converting $NO_3^-$ to $NO_2^-$, as the produced $NO_2^-$ (from $NO_3^-$ reduction) may be preserved as the final product on the electrode.

**Highly selective $NO_3^-$-to-$NO_2^-$ pathway on OD-Ag with enhanced activity.** In order to significantly enhance NO3RR activity, OD-Ag electrocatalysts were directly prepared from Ag foil by performing square wave voltammetry (SWV) and then conducting chronoamperometry (CA) under a constant negative potential.[22] The color change of Ag foil during the preparation was shown in Figure S2a and Supporting Information Movie S1. The chemical state change between $AgO_x$ and $Ag^0$ during synthesis and the successful formation of OD-Ag was confirmed by X-ray diffraction (XRD) spectroscopy (Figure S2b) and X-ray photoelectron spectroscopy (XPS) (Figure S2c).[23] Scanning electron microscope (SEM) imaging (Figure 2a) shows that OD-Ag has a rough surface with small particles (around 100 nm), in contrast to the smoother surface of Ag foil (Figure S3). Interestingly, optimized synthesis created a stepped and periodic wave-like morphology with ±250 nm of surface depth, which was confirmed by atomic force microscopy (AFM) analysis (Figure 2b and Figure S3a–d) and lower-magnification SEM images (Figure S3e–f). Underpotential deposition (UPD) of Pb[24] (Figure S4) showed OD-Ag has 27.1 $cm^2$ of electrochemical surface area (ECSA), or 13 times as much as the same geometric size of Ag foil (2.1 $cm^2$).

As shown in Figure 2c, compared with Ag foil, the onset potentials (NO3RR, NO2RR, and HER) on OD-Ag are positively shifted by approximately 200 mV, with the wide onset potential window still maintained. In particular, by comparing Figure 2c with Figure 1a, OD-Ag showed the widest potential difference between NO3RR and NO2RR (440 mV, blue region), as well as between NO3RR and HER (540 mV, blue + orange region), among the total 18 metals screened.

The superior $NO_3^-$-to-$NO_2^-$ activity on OD-Ag was confirmed by comparing with Ag foil and commercial nano-Ag catalyst (*i.e.*, Ag NPs/Ag: Ag nanoparticle-coated Ag foil). As can be seen from Figure S9b, throughout the potential range of −0.90 to −1.15 $V_{Ag/AgCl}$, OD-Ag delivered 5–10 times higher $NO_3^-$ conversion than Ag foil in the same electro-reduction experiment with the electrolyte containing 0.1 M $NO_3^-$ for one hour. More importantly, ultra-high faradaic efficiency (FE) towards $NO_2^-$ ranging from 95.4% to 91.3% and selectivity between 98.8% to 95.9% were obtained under the electrode potential from −0.90 V to −1.15 $V_{Ag/AgCl}$, accordingly (Figure S9c). In addition, the intrinsic activity of NO3RR was largely enhanced on the in-situ electrochemically fabricated OD-Ag, as confirmed by comparing OD-Ag with Ag NPs/Ag. As shown in Figure S10, under similar conditions (particle size, substrate, etc.), OD-Ag exhibited tripled area-specific activity (0.72 *vs.* 0.26 mA $cm^{-2}_{Ag}$) and over doubled $NO_3^-$ conversion (19.6% *vs.* 8.5%).

At lower $NO_3^-$ concentrations (0.05 and 0.01 M), as shown in Figure 2d, $NO_2^-$ production still dominated on OD-Ag with the $NO_3^-$-to-$NO_2^-$ selectivity all higher than 87.3% in the potential range of −1.00 to −1.30 $V_{Ag/AgCl}$, by applying the exact amount of theoretical charge (*i.e.*, 29 C) required to completely reduce 0.01 M $NO_3^-$ to $NO_2^-$. More negative potentials resulted in a gradual increase in $NH_4^+$ generation, while the charge consumption by HER remained insignificant for all tested conditions (FE: <10%, Figure S11). The high $NO_3^-$-to-$NO_2^-$ selectivity on OD-Ag was maintained in a wide potential window even with low $NO_3^-$ concentrations, indicating a robust and well-regulated transformation.

We also compared OD-Ag with the widely used Cu foil at −1.30 $V_{Ag/AgCl}$ under the same experimental conditions. With 0.01 M $NO_3^-$, it was found that OD-Ag outperformed Cu in both $NO_3^-$ conversion (65.3% *vs.* 39.0%) and $NO_3^-$-to-$NO_2^-$ selectivity (87.3% *vs.* 48.5%, Figure 2e). Their performance difference was further validated by tests under different $NO_3^-$ concentrations and strongly negative potential of −1.50 $V_{Ag/AgCl}$ (Figure S12). Control experiments (Figure S13) by replacing $KNO_3$ with $K^{15}NO_3$ have confirmed N source of produced $NH_4^+$ was derived from NO3RR, and the quantification of $NO_2^-$ was accurate as the approached selectivity measured by different analysis methods (liquid chromatography and colorimetry). The exceptionally high NO3RR selectivity to $NO_2^-$ on OD-Ag also outperforms many other reported Cu-based catalysts.[25-28]

As expected, the observed potential (−1.30 $V_{Ag/AgCl}$) of losing dominance (>90% selectivity) for $NO_3^-$-to-$NO_2^-$ is fairly consistent with the potential (−1.25 $V_{Ag/AgCl}$) that triggers the $NO_2^-$-to-$NH_4^+$ reaction at the same concentration of 0.01 M $NO_2^-$ solution (Figure S14). Interestingly, a detectable level of $NH_2OH$ showed up under relatively more negative potentials in NO3RR (Figure 2c). In addition, more $NH_2OH$ was generated from direct NO2RR (selectivity up to 5.6%, Figure S14). Such results are in concert with the recognition that $NH_2OH$ is a reaction intermediate to $NH_4^+$ for the reduction of $NO_3^-$ and $NO_2^-$.[29-30]

In addition to the high $NO_3^-$-to-$NO_2^-$ activity, OD-Ag appeared highly durable and robust under testing conditions. As evidenced by XPS and XRD spectra (Figure S15a–b), the chemical state of Ag in OD-Ag was unchanged

after the electrochemical measurements. Neither structural change nor Ag leaching was detected (Figure S15c–d). Moreover, no apparent loss of selectivity and FE of $NO_2^-$ was observed for four consecutive 1-hour measurements (Figure S15e).

**Mechanism and kinetics of NO3RR on OD-Ag.** To obtain more mechanistic insights into the electro-kinetics for $NO_3^-$-to-$NO_2^-$, the reaction order with respect to the $NO_3^-$ concentration was analyzed by fitting the partial current density for $NO_3^-$-to-$NO_2^-$ against the $NO_3^-$ concentration in log-log scale. Under −0.85 $V_{Ag/AgCl}$ (*i.e.*, 60 mV more negative than the onset potential), ~100% FE of $NO_3^-$ to $NO_2^-$ has been verified on OD-Ag in all tested $NO_3^-$ concentrations (0.010–0.100 M, adjusted to pH 4 for each case), allowing the LSV currents (Figure S16) of $NO_3^-$ reduction to be used as the partial currents for $NO_3^-$-to-$NO_2^-$. Note that the same reference electrode (Ag/AgCl) was used in all $NO_3^-$ concentrations to ensure accurate potential control, thanks to its pH-insensitive nature.[31] As shown in Figure 3a, a slope of 0.87 was obtained in the concentration range from 0.010 M to 0.075 M, strongly suggesting the first-order dependence of the $NO_3^-$-to-$NO_2^-$ reaction on the $NO_3^-$ concentration. The concentration of 0.100 M $NO_3^-$ does not follow the fitting, mainly due to the saturated active sites in $NO_3^-$ adsorption. The Tafel curves showed a slope of 120 mV $dec^{-1}$ (Figure S17), which corresponds to an empirical transfer coefficient ($\alpha = 2.303RT/F\ d\log(j)/dE$) of 0.48. This suggested the first-electron transfer involved in the RDS of $NO_3^-$-to-$NO_2^-$ reaction on OD-Ag.[32] Further, in the temperature range of 20–71 °C, a moderate apparent activation energy was obtained (15.8 kJ $mol^{-1}$, under −1.10 $V_{Ag/AgCl}$, Figure S18).

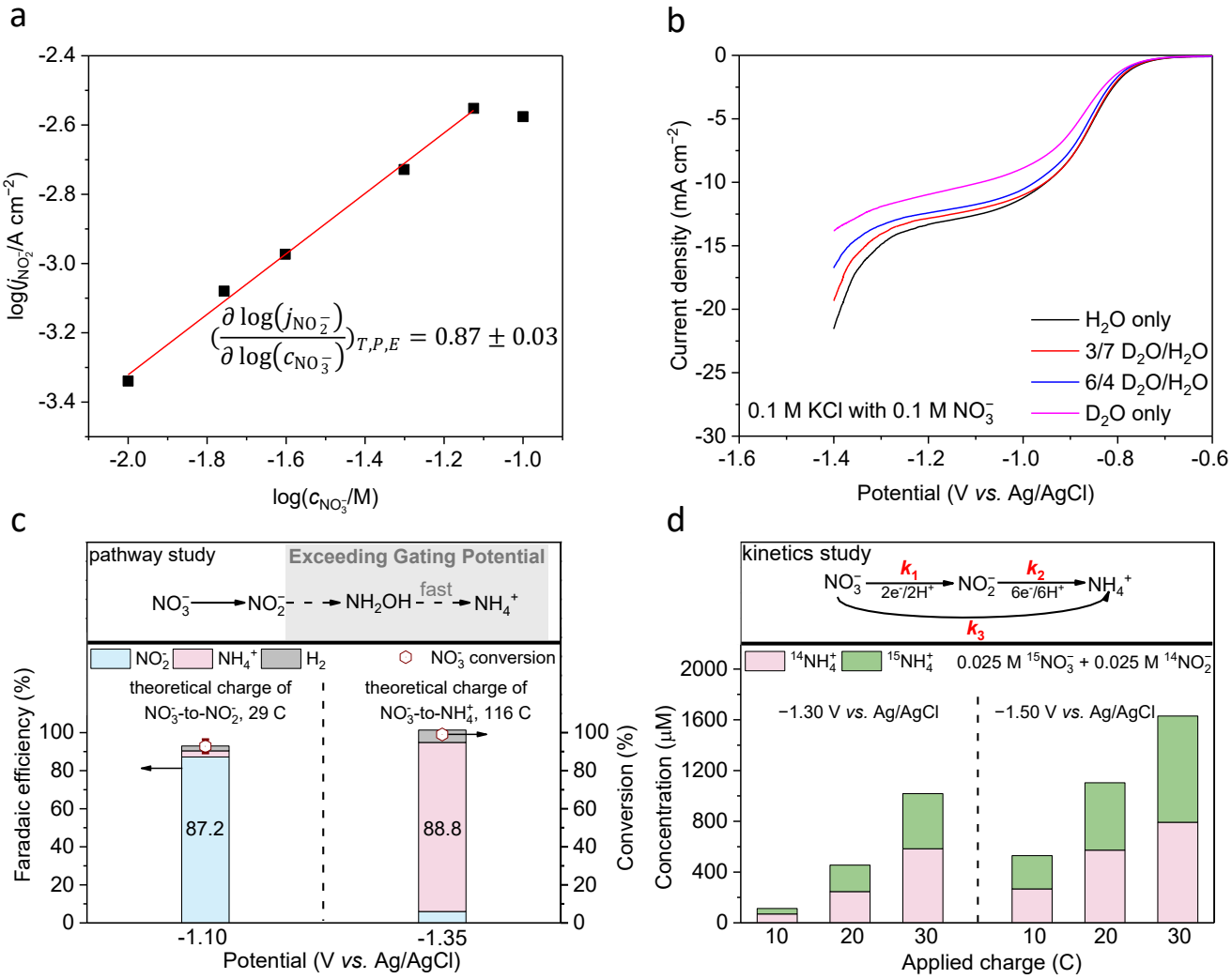


**Figure 3**. Kinetics and mechanism study of NO3RR on OD-Ag. (a) $NO_3^-$ order dependence fitting in 0.1 M KCl with different concentrations of $NO_3^-$ (pH = 4) at −0.85 $V_{Ag/AgCl}$ with data obtained from LSV curves in Figure S17. (b) LSV of OD-Ag in 0.1 M KCl with 0.1 M $NO_3^-$ at different ratios of $D_2O/H_2O$ as the solvent. (c) Faradaic efficiency and $NO_3^-$ conversion in 0.1 M KCl with 0.1 M of $NO_3^-$ (pH = 4) at −1.10 $V_{Ag/AgCl}$ and −1.35 $V_{Ag/AgCl}$. The applied charge was 29 C (the theoretical charge for $NO_3^-$-to-$NO_2^-$ reaction) and 116 C (the theoretical charge for $NO_3^-$-to-$NH_4^+$ reaction) at −1.10 $V_{Ag/AgCl}$ and −1.35 $V_{Ag/AgCl}$, respectively. The top inserted was the reaction pathway for NO3RR on OD-Ag. (d) Concentration of produced $^{14}NH_4^+$ and $^{15}NH_4^+$ in 0.1 M KCl containing 0.025 M $^{15}NO_3^-$ and 0.025 M $^{14}NO_2^-$ at the potential of −1.30 and −1.50 $V_{Ag/AgCl}$, respectively, with different applied charges. The isotopic products detection is detailed in the methods section, and their calibrations are shown in Figure S7.

In particular, the NO3RR pathway can be well regulated by the cathodic potential applied on OD-Ag. As shown in Figure 3c and Figure S19, by applying the theoretical charge (29 C) in converting 0.01 M $NO_3^-$ to $NO_2^-$ at −1.10 $V_{Ag/AgCl}$, the reaction kinetics (or the current density) was gradually decreased to zero during consumption of $NO_3^-$, in which the $NO_3^-$ conversion attained 92.8% with the observed $NO_2^-$ FE of 87.2%. Extending reaction time or applying excess charges under the same potential cannot overcome the activation obstacle for further reducing the accumulated $NO_2^-$ to $NH_4^+$ or triggering HER on OD-Ag. In sharp contrast, by applying a potential (−1.35 $V_{Ag/AgCl}$) more negative than the onset potential of NO2RR, 99.0% of $NO_3^-$ can be converted with an $NH_4^+$ FE of 88.8% via passing 116 C charge (the theoretical charge for $NO_3^-$-to-$NH_4^+$ reaction). The performance of the FE to $NH_4^+$ in the present work is competitive with or better than the state-of-the-art NO3RR electrocatalysts reported recently (detailed comparison in Table S2).

The high FE to $NH_4^+$ was benefited from the ultra-high activity of $NO_3^-$-to-$NO_2^-$ on OD-Ag since it has been confirmed in regulating the overall NO3RR pathway.[16-17] The above results further indicated a "gating potential" (or the potential starting to trigger $NO_2^-$ to $NH_4^+$ route) exists in the NO3RR pathway: exceeding the gating potentials, further reduction of accumulated $NO_2^-$ to $NH_4^+$ would have rapid kinetics and with HER still much suppressed. Furthermore, a series reduction pathway of $NO_2^-$-to-$NH_2OH$-to-$NH_4^+$ was proposed in this work (Figure 3c top inserted), based on the observation of the minor $NH_2OH$ and major $NH_4^+$ products during NO2RR (Figure S19) and the transformation of $NH_2OH$ to $NH_4^+$ with lower onset potential and facile kinetics (Figure S20).

Since two protons are involved in the $NO_3^-$-to-$NO_2^-$ reaction, H/D kinetic isotope effect (KIE) was studied by comparing the LSV in different solvents: pure $H_2O$, pure $D_2O$, and two ratios of mixtures on OD-Ag in 0.1 M $NO_3^-$-containing electrolyte. As shown in Figure 3b, a prominent isotopic effect was observed with a KIE value of 1.33 under −0.85 $V_{Ag/AgCl}$ (not a mass-transport-limited potential). Such observation implies that protons participated in the RDS of $NO_3^-$-to-$NO_2^-$ reaction, in agreement with the proton-assisted mechanism identified by DFT computations discussed in the next section.

$^{14}N/^{15}N$ isotopic experiments were designed and conducted to probe the $NO_3^-$ reduction kinetics and pathways on OD-Ag. Specifically, an equal concentration (0.025 M) of $^{15}NO_3^-$ and $^{14}NO_2^-$ was used in the solution medium, and two characteristic strongly negative electrode potentials (−1.30 and −1.50 $V_{Ag/AgCl}$) were investigated, under which considerable levels of $NH_4^+$ were generated. Enabled by the simultaneous detection of both isotopically labeled $^{14}NH_4^+$ and $^{15}NH_4^+$ by NMR spectroscopy (Figure 3d), the kinetics of the following three separate reactions can be revealed: $^{15}NO_3^-$ to $^{15}NO_2^-$ (reaction 1, $k_1$ as the apparent rate constant), $^{14}NO_2^-$ to $^{14}NH_4^+$ (reaction 2, $k_2$), and $^{15}NO_3^-$ to $^{15}NH_4^+$ (reaction 3, $k_3$). The detailed kinetic model derivation, data collection, and kinetics regressions analysis are shown in Supporting Information Note 1 and Figure S21.

As shown in Figure S21, $k_2$ (0.0064 $min^{-1}$) is approximately a quarter of $k_1$ (0.0273 $min^{-1}$) under −1.30 $V_{Ag/AgCl}$, while $k_3$ (0.0007 $min^{-1}$) is negligible. Under −1.50 $V_{Ag/AgCl}$, both $k_2$ and $k_3$ grew much more prominently than $k_1$. The $k_2$ and $k_3$ increased 4 times and 8 times, respectively, from −1.30 to −1.50 $V_{Ag/AgCl}$. As such, $k_2$ (0.0255 $min^{-1}$) and $k_3$ (0.0056 $min^{-1}$) attained about 81% and 18% of $k_1$, respectively. These calculated kinetic constants agreed well with the product selectivity observed from chronoamperometry (CA) tests.

More interestingly, $k_3$ is non-negligible under strongly negative potentials, indicating a $NO_3^-$-to-$NH_4^+$ reaction pathway that potentially "bypasses" the desorption of the reaction intermediate ($NO_2$*, the precursor of $NO_2^-$ product[33-34]) and directly turns into $NH_4^+$ product. This experimentally detected direct $NO_3^-$-to-$NH_4^+$ reaction pathway is consistent with the DFT calculation prediction noted by the recent work on a Cu-based catalyst.[35]

In addition, very low FE towards $NO_x$ gas products was detected from both NO3RR and NO2RR ($N_2O \leq 0.19\%$, $NO/NO_2 \leq 0.007\%$). Noted that these low amounts of $NO_x$ are detectable and can be accurately quantified, with the details shown in the Supporting Information and Table S3. These results excluded the possible side reactions to yield intermediate $NO_x$ products and also justified the reasonability of our kinetics model.

**DFT computations of NO3RR mechanism.** First-principles density functional theory (DFT) calculations[36-37] employing a simple electrochemical model[38] were performed to obtain a fundamental understanding of the experimental observations. As detailed in the computational methods, the adsorption of $NO_3^-$ to form $NO_3$* was calculated according to previous work;[39] this adsorption is potential dependent to account for the transfer of the electron upon adsorption. Two mechanisms were considered for the reduction of $NO_3$* to $NO_2$*, as the details leading to N–O bond scission have not been fully elucidated. In the first ("direct dissociation") pathway, an N–O bond in $NO_3$* is broken by the catalyst surface to form adsorbed $NO_2$* and O*. This does not involve the direct transfer of a proton-electron pair, so the calculated energetics are independent of potential. Due to anticipated difficulties with performing this on a weak-binding metal such as Ag, a second ("hydrogen assisted") pathway was considered in which a proton-electron pair is transferred to $NO_3$*, forming $HNO_3$*; this subsequently dissociates to form $NO_2$* and OH*. The dissociation of $HNO_3$* has very low barriers and is unaffected by potential. The O*/OH* formed by these two pathways are subsequently reduced to water.

We evaluated the detailed energetics of these two mechanisms for reduction of $NO_3$* and $NO_2$* on Ag(111), Cu(111), and Pd(111). We additionally performed calculations on Ag(211), which we selected as a simple approximation for OD-Ag due to the wave-like, amorphous structure exposing an increased fraction of

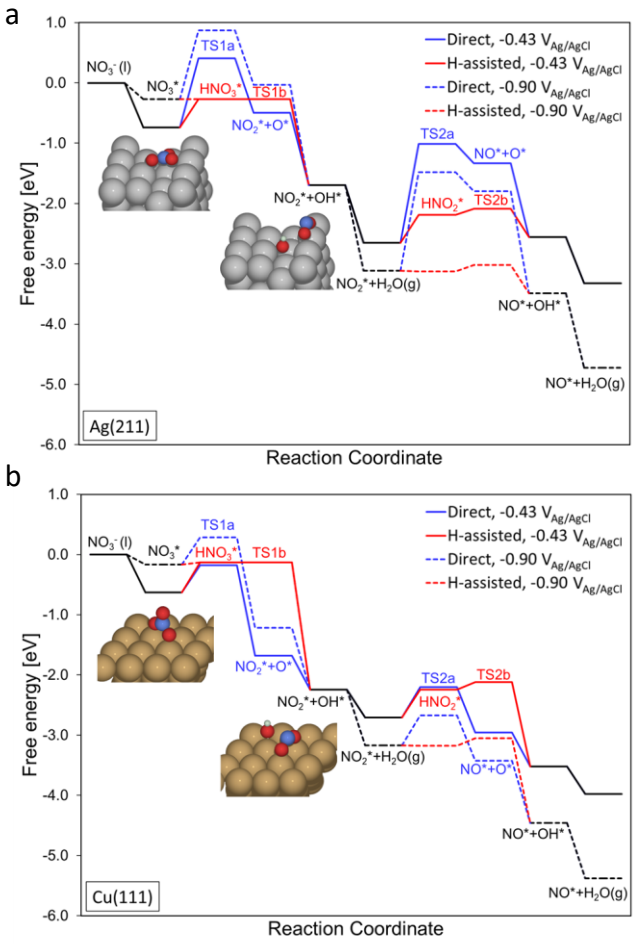


**Figure 4.** Energy diagrams of the considered reaction pathways of $NO_3^-$ reduction on (a) Ag(211) at 0.00 $V_{RHE}$, (b) Cu(111) at 0.00 $V_{RHE}$, (c) Ag(211) at −0.47 $V_{RHE}$, and (d) Cu(111) at −0.47 $V_{RHE}$. Shared states are shown in black. Transition states (TS) are labeled for $NO_3$* dissociation (TS1) and $NO_2$* dissociation (TS2). The most stable adsorption geometries of $NO_3$* and $NO_2$* + OH* on Ag(211) and Cu(111) are shown in the diagrams, with atom colors: Ag (grey), Cu (brown), H (white), N (blue), O (red).

undercoordinated sites.[40-41] Although we do not have direct experimental evidence of the undercoordinated sites on OD-Ag, due to the challenge of performing HRTEM on a bulk foil-based material, we note that its largely enhanced ECSA implies a lower average degree of atomic coordination. Further, the nature of the synthesis (high-frequency electrochemical oxidation-reduction treatment) is anticipated to leave a rough, undercoordinated surface. Direct comparisons are made here between Ag(211) and Cu(111); Ag(111) and Pd(111) data are presented in Table S4. We note that detailed activation energies were not calculated for all N–O bond breaking steps on Ag(111) and Pd(111), as we focused our analysis on understanding the interesting selectivity differences between OD-Ag and Cu foil.

The calculated reaction energetics at 0.00 $V_{RHE}$ on Ag(211) and Cu(111) are presented in Figure 4 (a) and (b). These results show that the direct dissociation of $NO_3$* on Ag(211) is highly activated (1.14 eV). Notably, the H-assisted pathway occurring by first forming adsorbed $HNO_3$* is substantially more favorable than forming the transition state for direct dissociation (TS1a), even under mild reducing potentials (0.46 eV at 0.00 $V_{RHE}$), and the dissociation of $HNO_3$* (TS1b) is spontaneous (activation free energy of 0.00 eV). This illustrates a key advantage of the H-assisted mechanism over direct dissociation; the favorability of $HNO_3$* formation increases as the potential becomes more negative, decreasing the effective barrier to N–O bond breaking.

Our results show that a similar mechanism holds for the second reduction of adsorbed $NO_2$*: direct dissociation on Ag(211) also has a high activation energy (1.64 eV), but the formation of $HNO_2$* (0.46 eV at 0.00 $V_{RHE}$) enables a lower-energy dissociation (0.10 eV). The dissociation of $HNO_2$* therefore has a slightly higher energy barrier than $HNO_3$* dissociation on Ag(211).

We compared the Ag(211) results with those obtained on Cu(111) (Figure 4b) and found that Cu(111) has more favorable activation energy barriers for direct dissociation of $NO_3$* (0.45 eV) and $NO_2$* (0.50 eV) than does Ag(211) (1.14 eV and 1.64 eV, respectively). This suggests some feasibility of direct dissociation on Cu(111), though rates will be relatively slow due to these larger barriers. The H-assisted pathways at 0.00 $V_{RHE}$ on Cu(111) have effective barriers comparable in magnitude to the corresponding direct dissociations of both $NO_3^-$ and $NO_2^-$, though the H-assisted pathways again become more favorable and dominate at more negative potentials. A detailed comparison of the reaction energetics between Ag(211) and Cu(111) is presented in Figure S22 to emphasize the difference of energetics between the metal surfaces for each mechanism.

The energetics on both surfaces at −0.90 $V_{Ag/AgCl}$ are presented Figure 4 (c) and (d), after adjusting the computational reference potential from RHE to Ag/AgCl (KCl saturated, $E^0$ = 0.197 V *vs.* SHE) in pH 4 electrolyte ($E_{RHE}$ = −0.467 V under this condition; see methods section for details). This figure clearly shows the favorability of the H-assisted mechanisms on both Ag(211) and Cu(111) at more reducing potentials. We calculate that the energetics of $HNO_3$* formation are energetically favorable (*i.e.*, $\Delta G < 0$ for all elementary steps) at potentials more negative than −0.90 $V_{Ag/AgCl}$ on Ag(211) and −0.94 $V_{Ag/AgCl}$ on Cu(111). These values correspond well, considering the approximate nature of our surface models, to the experimentally-observed onset potentials for NO3RR at roughly −0.79 V and −0.94 V on OD-Ag and Cu foil, respectively, offering an explanation for the strong reducing potentials required for experimental activity. Since all electrochemical steps have favorable energetics (*i.e.*, $\Delta G < 0$) under potentials more negative than these onset potentials, $HNO_3$* dissociation (which is not an electrochemical step) becomes rate-determining along the preferred H-assisted pathway to forming $NO_2^-$. Further, we note that the activation enthalpy of this potential-independent step (Table S7) on Ag(211) (0.12 eV, 11.6 kJ mol$^{-1}$) is consistent with the experimental apparent activation energy discussed above for OD-Ag (15.8

kJ $mol^{-1}$ at −1.10 $V_{Ag/AgCl}$). These computational results indeed suggest that the electrochemical active site is likely to be relatively undercoordinated in nature, due to the consistency of our model and experimental results.

Our DFT calculations also provide insight into the reasons for the high $NO_3^-$-to-$NO_2^-$ selectivity observed on OD-Ag that was not prominent on Cu foil, which relates to the relative energies of dissociating $NO_3$* and $NO_2$* through the respective H-assisted pathways. The free energy of forming the $HNO_2$* transition state (TS2b) relative to $NO_2$* is 0.10 eV more difficult than forming the $HNO_3$* transition state (TS1b) from $NO_3$* on Ag(211). In contrast, forming TS2b is only 0.08 eV more difficult than forming TS1b from the respective states on Cu(111). This facilitates the relative dissociation rate of $HNO_2$* on Cu(111) and prevents $NO_2^-$ from being the dominant product. More significantly, $NO_2$* is also bound 0.05 eV more weakly on Ag(211) than on Cu(111) (Table S5–6). Together, these suggest fundamental reasons for the ability of OD-Ag to desorb $NO_2^-$ relative to Cu foil, which instead further reduces $NO_2$* to $NH_4^+$. Though the differences in energetics are small, we note that 0.06 eV represents roughly an order of magnitude difference in rate constants at room temperature. Overall, the decomposition of $NO_3$* has more favorable kinetics than that of $NO_2$*; this agrees with the experimental findings of a higher apparent rate constant $k_1$ compared to $k_2$ on OD-Ag.

The remaining electrochemical steps to form $NH_3$ were calculated to be energetically favorable after the dissociation of $HNO_2$* to form NO*; in fact, a pathway exists such that all steps are more favorable than the corresponding NO3RR and NO2RR electrochemical steps (Figure S23–24). This is in agreement with our expectation that N-O bond breaking in $NO_3$* is rate-determining, and the experimental observation that $NO_2^-$ and $NH_4^+$ are nearly exclusively the only products formed. Additional factors may influence the relative reduction activities on the considered surfaces. First, the relatively strong adsorption of $NO_3$* on Ag(211) (0.11 eV stronger than Cu(111), see Tables S4–5) increases its coverage and the reaction rate; $NO_3^-$ adsorption has been previously reported to limit the $NO_3^-$-to-$NO_2^-$ reaction.[42-43] Second, hydrogen competes for surface sites with $NO_3$* and decreases its coverage.[10, 42] The free energy of atomic hydrogen on all surfaces was more negative than that on Ag(211), suggesting another reason for the favorable $NO_3^-$ reduction properties on OD-Ag relative to Cu(111), Pd(111), and Ag(111). We also note the relatively strong adsorption of O* and OH* on Cu(111), which hinders the ability to recover free sites through proton-electron addition, reducing the observed activity and onset potential.[10] We note that the potential dependent selectivities to $NO_2^-$ and $NH_4^+$ were not quantitatively elucidated in the theoretical study, likely due the simple nature of the model (Ag(211), and other assumptions noted below). We additionally omit other reduction mechanisms corresponding to interactions between other adsorbed species. Still, the energetics detailed above offer crucial insights into the reduction onset potential and relative $NO_3^-$-to-$NO_2^-$ of OD-Ag and Cu foil.

It is additionally meaningful to compare energetics on Ag(211) with those on Ag(111) to understand the intrinsic structure sensitivity on Ag and the relatively low activity of Ag foil (see Tables S4-S5 and S7). The calculated activation energies of N-O bond dissociation via the H-assisted pathway are very similar (0.12 eV on Ag(211), 0.13 eV on Ag(111)); we highlight two possible explanations that surface coverage effects dominate the relative activities of these surfaces, rather than N-O dissociation kinetics. First, the calculated adsorption free energies of $NO_3$* were −0.27 eV on Ag(211) and +0.10 eV on Ag(111) at −0.90 $V_{Ag/AgCl}$, demonstrating the relative difficulty of nitrate uptake on Ag(111). Second, H* adsorbs 0.06 eV more strongly on Ag(111) than on Ag(211); as discussed above, strong adsorption of H* can reduce the availability of active sites for $NO_3$* adsorption and dissociation.

Other factors not considered here influence the quantitative agreement between modeling and experiments, and should be considered in future studies. Potential-dependent activation energy barriers for electrochemical steps were neglected similar to previous work;[44-45] although we calculate that this is reasonable at the strong reducing conditions used in this study (see Supporting Information Note 2), these barriers will be more relevant at lower overpotentials desirable in future designed catalysts.[46] Briefly, other limitations involve the inclusion of solvent effects on energies of intermediates and transition states,[47] and surface coverage effects.[48] Our computational insights are nevertheless in good agreement with our experimental results showing superior electrocatalytic performance on OD-Ag for $NO_3^-$-to-$NO_2^-$ reduction relative to Cu(111), Pd(111), and Ag(111).

**A combined electrocatalytic-catalytic process for $NO_3^-$ removal from agricultural waste streams.** Apart from recycling $NO_3^-$ into $NH_4^+$ as a useful chemical, it is desirable in other circumstances (*e.g.*, drinking water processing) to return the fixed nitrogen to the atmosphere in the form of inert $N_2$ as the final step of closing the nitrogen cycle. However, the direct one-step electrocatalytic $NO_3^-$-to-$N_2$ reaction has proved challenging and kinetically unfavorable.[12-13] Herein, built on the discovered exceptionally-high $NO_3^-$-to-$NO_2^-$ selectivity (up to 98%) and conversion (>95%) on OD-Ag, we propose a combined electrocatalytic-catalytic process for $NO_3^-$ removal from agricultural waste streams by coupling the electrocatalytic $NO_3^-$-to-$NO_2^-$ step on OD-Ag with the subsequent catalytic $NO_2^-$-to-$N_2$ step on a Pd catalyst using $H_2$ that is generated on-site by a PEM-based water electrolyzer (Figure 5a and Figure S25).

Pd is one of the most active metals to efficiently catalyze the reduction of $NO_2^-$ by $H_2$ at room temperature and ambient pressure,[49-50] particularly showing much more facile kinetics and favorable $N_2$ selectivity than direct reduction of $NO_3^-$, which has been extensively studied on Pd-based catalysts; however, minimizing $NH_4^+$ generation and increasing $NO_3^-$ reduction activity remains a challenge. The development of catalyst for $NO_2^-$ reduction is not in the scope of this work, and we only employed a commercial

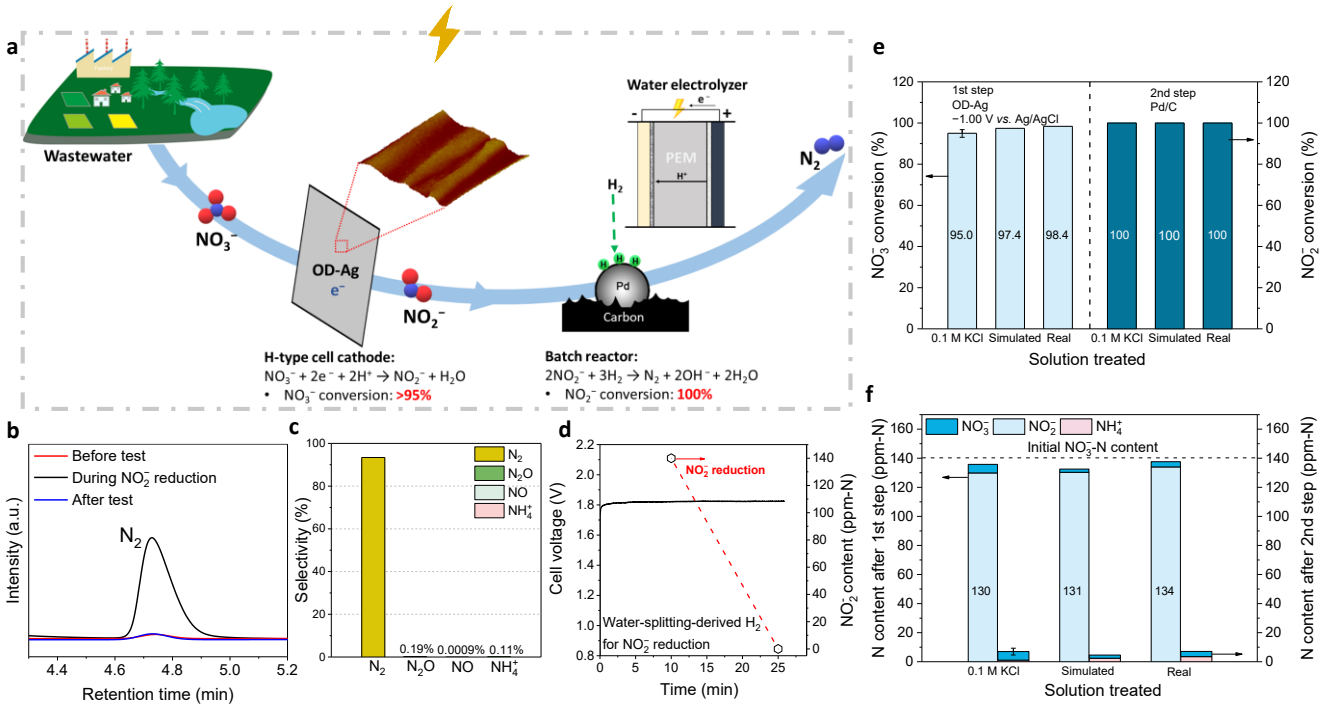


**Figure 5.** Nitrate removal by the combined electrocatalytic-catalytic process. Three solution media were tested: 0.1 M KCl, simulated waste stream from ion-exchange columns, and real-world agricultural wastewater (collected from Des Moines Water Works, Iowa), all of which were enriched to contain 0.01 M $NO_3^-$ (*i.e.*, 140 ppm-N). (a) The system components of the two-step combined process: electrochemical $NO_3^-$-to-$NO_2^-$ reaction, $NO_2^-$-to-$N_2$ reaction, and a PEM-based water electrolyzer to produce $H_2$ for $NO_2^-$ reduction in the batch reactor. $CO_2$ was fed during the test to maintain a constant pH.[9] (b) On-line GC to detect products from the catalytic reduction of 0.5 M $NO_2^-$ during different experimental periods. The retention time of $N_2$ was at around 4.7 min. (c) Product selectivity of catalytic reduction of 0.5 M $NO_2^-$ for 2 h. The details were shown in the methods section. (d) Voltage profile of the PEM electrolyzer at 1.4 A, and the $NO_2^-$ concentration before and after the reaction. At $t$ = 10–25 min, the gas outlet of the sealed cathode water tank was connected to the cell for $NO_2^-$ reduction. (e) $NO_3^-$ conversion on OD-Ag at −1.00 $V_{Ag/AgCl}$ in the first step (left part), and $NO_2^-$ conversion on Pd/C by $H_2$ in the second step (right part). The error bars represent the standard deviation for at least three independent measurements. (f) The compositions of N-containing compounds in the wastewater after the first (electrocatalytic) step and second (catalytic) step of the treatment. The detailed experimental results and some other test conditions are summarized in Table S11.

low-Pd-loading carbon-supported Pd catalyst (5 wt.% Pd/C) here. Concentrated $NO_2^-$ solution (0.5 M) was bubbled by $H_2$ for 2 hours in order to increase gas product intensity that can be accurately quantified. Highly selectively produced $N_2$ and minimized $NO_x$ gases through catalytic reaction were confirmed by different analysis methods. On-line gas chromatography (GC) confirmed 93.4% selectivity was towards $N_2$ (Figure 5b–c), and the selectivity towards $NH_4^+$, NO, and $N_2O$ were all <0.5% (Figure S26a and Table S9), based on colorimetry and off-line GC methods. The detailed product quantification and analyses were shown in the Supporting Information. In light of the possible adsorption of $NH_4^+$ or $NO_2^-$ on the porous carbon support,[51] control experiments elucidated negligible adsorption effect and importance of $CO_2$ buffering in our catalytic system (Figure S27).

The kinetics of catalytic reaction for $NO_2^-$-to-$N_2$ using $H_2$ was examined on Pd/C in 0.01 M $NO_2^-$, and a pseudo-first-order behavior was observed with a very high coefficient of determination ($R^2$ = 0.99, Figure S26b), leading to the Pd-normalized and surface-Pd normalized rate constant of 3.06 and 27.96 L $g_{Pd}^{-1}$ $min^{-1}$, respectively. In fact, it took only 5 min for Pd/C to remove >99% of 0.01 M $NO_2^-$. No apparent drop in catalytic performance was observed in three consecutive operations on Pd/C (Figure S26c).

To examine the robust $NO_3^-$-removal capability, the combined electrocatalytic-catalytic process was tested to treat three solution media: 0.1 M KCl, a simulated waste stream from ion-exchange columns,[52] and real-world agricultural wastewater (collected from Des Moines Water Works, Iowa), all of which were enriched to contain 0.01 M $NO_3^-$ (*i.e.*, 140 ppm-N). LSV showed no significant difference in the three solution media (Figure S28). After the combined process for water treatment, 95+% of $NO_3^-$ was converted with <3.5 ppm of $NH_4^+$-N and <5.9 ppm of $NO_3^-$-N remained, and no $NO_2^-$-N was detected in any of the treated solutions (Figure 5b). Detailed experimental results and other tested reaction conditions are summarized in Table S10. The combined denitrification process in this work presents one of the lowest undesirable selectivity towards $NH_4^+$ and one of the highest desirable selectivities towards $N_2$ among other reported catalytic/electrocatalytic processes, as

shown in Table S11. In particular, the combined process presented in our work outperformed a conventional two-step electrochemical $NO_3^-$-to-$N_2$ route (electrocatalytic reduction of $NO_3^-$-to-$NH_4^+$ coupled with the oxidation of $NH_4^+$-to-$N_2$)[13, 53] from an electron efficiency aspect, as the valence of N in their process went through the highest +5 to the lowest –3 and re-oxidized back to 0.

In addition, we have experimentally demonstrated that $H_2$ generated on-site by a PEM-based water electrolyzer can completely replace the $H_2$ feed from the pressurized cylinder (Figure 5d and Figure S29), avoiding the use of commercial $H_2$ which not only relies heavily upon the reforming of fossil fuels for production[54] but also requires costly infrastructure for storage and transportation.[55]

Considering that the pH of wastewater from different sources may vary,[56] we examined the electrocatalytic performance of OD-Ag in the pH range of 4.0–13.0 and observed a zeroth-order dependence on $H^+$ concentration (Figure S30–31). Besides, as from both the LSV and 1-hour CA or chronopotentiometry (CP) measurements (Figure S31–32), the potential-regulated ultra-high FE of $NO_2^-$ preserved in a broad range of pH on OD-Ag. In addition, the excellent electrocatalytic $NO_3^-$-to-$NO_2^-$ activity on OD-Ag in the H-type cell is transferable to a flow reactor for its continuous conversion (Figure S33). Based on the flow demonstration, a simple technoeconomic analysis (TEA) was conducted on the electrocatalytic-catalytic combined process driven by renewable electricity (Supporting Information Note 4). The estimated capital cost for removing $NO_3^-$-containing wastewater to $N_2$ was 0.026 $ per $m^3$ in our combined process, which is competitive or outperformed other treatment methods (Table S12).[57] To sum up, our tandem wastewater treatment process is operable in a wide pH range, resistible to interferences of different possible impurities (cations, anions, and microbes) in real wastewater, and holds promising economic feasibility.

We note that $NO_2^-$ is a more toxic species than $NO_3^-$ in drinking water, however $NO_2^-$ could be utilized as the intermediate product, as long as $NO_2^-$ can be quickly and completely converted to safe end products.[58-59] As demonstrated in Figure 5, 100% of $NO_2^-$ conversion was readily attained for all wastewater media, while the conversion of $NO_3^-$ on the same commercial Pd/C catalyst was negligible (<1%, Figure S27c–d). In addition to the wastewater treatment to $N_2$, $NO_2^-$ derived from nitrate may serve as a crucial reactive platform for distributed production of various nitrogen products, such as NO,[60] $NH_2OH$, $NH_3$,[61-62] and urea.[63]

## CONCLUSION

In this work, we discovered the unique and ultra-high $NO_3^-$-to-$NO_2^-$ activity on OD-Ag, with up to 98% selectivity and 95% FE were achieved and well-maintained in a wide potential window. Electro-kinetics has identified the reduction of $NO_3^-$ to $NO_2^-$ or further reduction of $NO_2^-$ to $NH_4^+$ is well regulated by cathodic potential on OD-Ag. DFT computations provided mechanistic insights into the ultrahigh $NO_3^-$-to-$NO_2^-$ selectivity observed on OD-Ag, which was not prominent on Cu. Built on the efficient pathway, we have demonstrated a novel combined process for $NO_3^-$ removal by coupling the electrocatalytic $NO_3^-$-to-$NO_2^-$ step on OD-Ag with the subsequent catalytic $NO_2^-$-to-$N_2$ step on a Pd catalyst using $H_2$ generated on-site by a PEM-based water electrolyzer, resulting in 95+% of $NO_3^-$ removal from the 0.01 M $NO_3^-$-containing real-world agriculture wastewater. Moreover, different N-containing intermediates ($NO_2$, $NO_2^-$, NO, $N_2O$, $N_2$, $NH_2OH$, $NH_4^+$) have been analyzed and quantified via different on-line or off-line methods in our work, with accurate nitrogen balances (~95%) were established for both electrocatalytic and catalytic processes. Powered by inexpensive renewable electricity, the directional reduction of $NO_3^-$ might unlock the potential to denitrify agricultural wastewater towards utterly harmless $N_2$ or economically valuable $NH_3$. The produced $NO_2^-$ may also be utilized as a reactive platform species for distributed manufacturing of various nitrogen-based products in need.

## AUTHOR INFORMATION


### Corresponding Author

**Wenzhen Li –** Department of Chemical and Biological Engineering, Iowa State University, 618 Bissell Road, Ames, Iowa 50011, United States; ORCID: 0000-0002-1020-5187; Email: wzli@iastate.edu

**Luke T. Roling** – Department of Chemical and Biological Engineering, Iowa State University, 618 Bissell Road, Ames, Iowa 50011, United States; ORCID:0000-0001-9742-2573; Email: roling@iastate.edu

### Authors

**Hengzhou Liu –** Department of Chemical and Biological Engineering, Iowa State University, 618 Bissell Road, Ames, Iowa 50011, United States

**Jaeryul Park –** Department of Chemical and Biological Engineering, Iowa State University, 618 Bissell Road, Ames, Iowa 50011, United States

**Yifu Chen –** Department of Chemical and Biological Engineering, Iowa State University, 618 Bissell Road, Ames, Iowa 50011, United States

**Yang Qiu –** Institute for Integrated Catalysis, Energy and Environment Directorate, Pacific Northwest National Laboratory, 902 Battelle Blvd., Richland, Washington 99352, United States

**Yan Cheng –** Department of Chemical and Biological Engineering, Iowa State University, 618 Bissell Road, Ames Iowa 50011, United States

**Kartik Srivastava –** Department of Chemical and Biological Engineering, Iowa State University, 618 Bissell Road, Ames, Iowa 50011, United States

**Shuang Gu –** Department of Mechanical Engineering, Wichita State University, 1845 Fairmount St, Wichita, Kansas 67260, United States

**Brent H. Shanks –** Department of Chemical and Biological Engineering, Iowa State University, 618 Bissell Road, Ames, Iowa 50011, United States


### Notes

The authors declare no competing financial interest.

## ASSOCIATED CONTENT

This supporting information is available free of charge via the Internet at http://pubs.acs.org."

Experimental details, supporting figures and tables, and characterization data (PDF)

## ACKNOWLEDGMENT

This work was supported in part by the NSF through the Future Manufacturing program (ChE 2036944). We thank Drs. Dapeng Jing, Curtis L. Mosher, Warren E. Straszheim, and Patrick A. Johnston for their assistance with XPS, AFM, SEM, and ICP-OES measurements, and Jeff Mitchell from Des Moines Water Works for supplying agricultural wastewater. We also acknowledge Dr. Myeongseong Lee and Dr. Jacek A. Koziel for their GC test for $N_2O$ quantification. W. Li is grateful to his Bailey Research Career Development Award and his Richard Seagrave Professorship. L. T. Roling recognizes support from the Michael and Denise Mack Fellowship. Computations were partially supported by the HPC@ISU equipment at Iowa State University, some of which was purchased through funding provided by the NSF under MRI grant number 1726447.

## REFERENCES

(1) Council, N. R., *Clean Coastal Waters: Understanding and Reducing the Effects of Nutrient Pollution*. The National Academies Press: Washington, DC, 2000; p 428.

(2) Ward, M. H.; DeKok, T. M.; Levallois, P.; Brender, J.; Gulis, G.; Nolan, B. T.; VanDerslice, J., Workgroup report: drinking-water nitrate and health—recent findings and research needs. *Environ. Health Perspect.* **2005,** *113* (11), 1607–1614.

(3) Ward, M. H.; Jones, R. R.; Brender, J. D.; de Kok, T. M.; Weyer, P. J.; Nolan, B. T.; Villanueva, C. M.; van Breda, S. G., Drinking Water Nitrate and Human Health: An Updated Review. *Int. J. Environ. Res. Public Health* **2018,** *15* (7), 1557.

(4) Temkin, A.; Evans, S.; Manidis, T.; Campbell, C.; Naidenko, O. V., Exposure-based assessment and economic valuation of adverse birth outcomes and cancer risk due to nitrate in United States drinking water. *Environ. Res.* **2019,** *176*, 108442.

(5) Gude, V. G., Wastewater treatment in microbial fuel cells–an overview. *J. Clean. Prod.* **2016,** *122*, 287–307.

(6) Park, J. Y.; Yoo, Y. J., Biological nitrate removal in industrial wastewater treatment: which electron donor we can choose. *Appl. Microbiol. Biotechnol.* **2009,** *82* (3), 415–429.

(7) Ghafari, S.; Hasan, M.; Aroua, M. K., Bio-electrochemical removal of nitrate from water and wastewater--a review. *Bioresour. Technol.* **2008,** *99* (10), 3965–3974.

(8) J. Schoeman, A. S., Nitrate removal with reverse osmosis in a rural area in South Africa. *Desalination* **2003,** *155*, 15–26.

(9) Samatya, S.; Kabay, N.; Yüksel, Ü.; Arda, M.; Yüksel, M., Removal of nitrate from aqueous solution by nitrate selective ion exchange resins. *React. Funct. Polym.* **2006,** *66* (11), 1206–1214.

(10) Martínez, J.; Ortiz, A.; Ortiz, I., State-of-the-art and perspectives of the catalytic and electrocatalytic reduction of aqueous nitrates. *Appl. Catal. B* **2017,** *207*, 42–59.

(11) Duca, M.; Koper, M. T., Powering denitrification: the perspectives of electrocatalytic nitrate reduction. *Energy Environ. Sci.* **2012,** *5* (12), 9726–9742.

(12) Fajardo, A. S.; Westerhoff, P.; Sanchez-Sanchez, C. M.; Garcia-Segura, S., Earth-abundant elements a sustainable solution for electrocatalytic reduction of nitrate. *Appl. Catal. B* **2021,** *281*, 119465.

(13) Garcia-Segura, S.; Lanzarini-Lopes, M.; Hristovski, K.; Westerhoff, P., Electrocatalytic reduction of nitrate: Fundamentals to full-scale water treatment applications. *Appl. Catal. B* **2018,** *236*, 546–568.

(14) Canfield, D. E.; Glazer, A. N.; Falkowski, P. G., The evolution and future of Earth's nitrogen cycle. *Science* **2010,** *330* (6001), 192–196.

(15) Rosca, V.; Duca, M.; de Groot, M. T.; Koper, M. T., Nitrogen cycle electrocatalysis. *Chem. Rev.* **2009,** *109* (6), 2209–2244.

(16) Wang, Z.; Richards, D.; Singh, N., Recent discoveries in the reaction mechanism of heterogeneous electrocatalytic nitrate reduction. *Catal. Sci. Technol.* **2021,** *11* (3), 705–725.

(17) Siriwatcharapiboon, W.; Kwon, Y.; Yang, J.; Chantry, R.; Li, Z.; Horswell, S.; Koper, M., Promotion effects of Sn on the electrocatalytic reduction of nitrate at Rh nanoparticles. *ChemElectroChem* **2014,** *1* (1), 172–179.

(18) Van Langevelde, P. H.; Katsounaros, I.; Koper, M. T., Electrocatalytic nitrate reduction for sustainable ammonia production. *Joule* **2021,** *5* (2), 290–294.

(19) Zeng, Y.; Priest, C.; Wang, G.; Wu, G., Restoring the Nitrogen Cycle by Electrochemical Reduction of Nitrate: Progress and Prospects. *Small Methods* **2020,** *4* (12), 2000672.

(20) Hao, D.; Chen, Z.; Figiela, M.; Stepniak, I.; Wei, W.; Ni, B.-J., Emerging alternative for artificial ammonia synthesis through catalytic nitrate reduction. *J. Mater. Sci. Technol.* **2020,** 163–168.

(21) Chen, G.-F.; Yuan, Y.; Jiang, H.; Ren, S.-Y.; Ding, L.-X.; Ma, L.; Wu, T.; Lu, J.; Wang, H., Electrochemical reduction of nitrate to ammonia via direct eight-electron transfer using a copper–molecular solid catalyst. *Nat. Energy* **2020,** *5* (8), 605–613.

(22) Ma, M.; Trześniewski, B. J.; Xie, J.; Smith, W. A., Selective and efficient reduction of carbon dioxide to carbon monoxide on oxide - derived nanostructured silver electrocatalysts. *Angew. Chem.* **2016,** *128* (33), 9900–9904.

(23) Murray, B.; Li, Q.; Newberg, J.; Menke, E.; Hemminger, J.; Penner, R., Shape-and size-selective electrochemical synthesis of dispersed silver (I) oxide colloids. *Nano Lett.* **2005,** *5* (11), 2319–2324.

(24) Kim, C.; Jeon, H. S.; Eom, T.; Jee, M. S.; Kim, H.; Friend, C. M.; Min, B. K.; Hwang, Y. J., Achieving Selective and Efficient Electrocatalytic Activity for $CO_2$ Reduction Using Immobilized Silver Nanoparticles. *J. Am. Chem. Soc.* **2015,** *137* (43), 13844–13850.

(25) Wang, Y.; Xu, A.; Wang, Z.; Huang, L.; Li, J.; Li, F.; Wicks, J.; Luo, M.; Nam, D.-H.; Tan, C.-S., Enhanced Nitrate-to-Ammonia Activity on Copper–Nickel Alloys via Tuning of Intermediate Adsorption. *J. Am. Chem. Soc.* **2020,** *142* (12), 5702–5708.

(26) Reyter, D.; Bélanger, D.; Roué, L., Study of the electroreduction of nitrate on copper in alkaline solution. *Electrochim. Acta* **2008,** *53* (20), 5977–5984.

(27) Yoshioka, T.; Iwase, K.; Nakanishi, S.; Hashimoto, K.; Kamiya, K., Electrocatalytic reduction of nitrate to nitrous oxide by a copper-modified covalent triazine framework. *J. Phys. Chem. C* **2016,** *120* (29), 15729–15734.

(28) Pérez-Gallent, E.; Figueiredo, M. C.; Katsounaros, I.; Koper, M. T. M., Electrocatalytic reduction of Nitrate on Copper single crystals in acidic and alkaline solutions. *Electrochim. Acta* **2017,** *227*, 77–84.

(29) Wang, Y., Zhou, W., Jia, R., Yu, Y. & Zhang, B. Unveiling the activity origin of a copper-based electrocatalyst for selective nitrate reduction to ammonia. *Angew. Chem. Int. Ed.* **2020,** *59,* 5350–5354.

(30) Shen, J.; Birdja, Y. Y.; Koper, M. T., Electrocatalytic nitrate reduction by a cobalt protoporphyrin immobilized on a pyrolytic graphite electrode. *Langmuir* **2015,** *31* (30), 8495–8501.

(31) Eliaz, N.; Gileadi, E., *Physical Electrochemistry: Fundamentals, Techniques, and Applications*. John Wiley & Sons: 2019.
(32) Bard, A. J.; Faulkner, L. R., Fundamentals and applications. *Electrochemical Methods* **2001,** *2* (482), 580–632.
(33) Dima, G.; De Vooys, A.; Koper, M., Electrocatalytic reduction of nitrate at low concentration on coinage and transition-metal electrodes in acid solutions. *J. Electroanal. Chem.* **2003,** *554*, 15–23.
(34) Dima, G.; Beltramo, G.; Koper, M., Nitrate reduction on single-crystal platinum electrodes. *Electrochim. Acta* **2005,** *50* (21), 4318–4326.
(35) Chen, G.-F.; Yuan, Y.; Jiang, H.; Ren, S.-Y.; Ding, L.-X.; Ma, L.; Wu, T.; Lu, J.; Wang, H., Electrochemical reduction of nitrate to ammonia via direct eight-electron transfer using a copper–molecular solid catalyst. *Nat. Energy* **2020**, 1–9.
(36) Kresse, G.; Furthmüller, J., Efficient iterative schemes for ab initio total-energy calculations using a plane-wave basis set. *Phys. Rev. B* **1996,** *54* (16), 11169.
(37) Kresse, G.; Furthmüller, J., Efficiency of ab-initio total energy calculations for metals and semiconductors using a plane-wave basis set. *Comput. Mater. Sci.* **1996,** *6* (1), 15–50.
(38) Nørskov, J. K.; Rossmeisl, J.; Logadottir, A.; Lindqvist, L.; Kitchin, J. R.; Bligaard, T.; Jonsson, H., Origin of the overpotential for oxygen reduction at a fuel-cell cathode. *J. Phys. Chem. B.* **2004,** *108* (46), 17886–17892.
(39) Calle-Vallejo, F.; Huang, M.; Henry, J. B.; Koper, M. T.; Bandarenka, A. S., Theoretical design and experimental implementation of Ag/Au electrodes for the electrochemical reduction of nitrate. *Phys. Chem. Chem. Phys.* **2013,** *15* (9), 3196–3202.
(40) Pander III, J. E.; Ren, D.; Huang, Y.; Loo, N. W. X.; Hong, S. H. L.; Yeo, B. S., Understanding the Heterogeneous Electrocatalytic Reduction of Carbon Dioxide on Oxide - Derived Catalysts. *ChemElectroChem* **2018,** *5* (2), 219–237.
(41) Back, S.; Yeom, M. S.; Jung, Y., Active sites of Au and Ag nanoparticle catalysts for $CO_2$ electroreduction to CO. *ACS Catal.* **2015,** *5* (9), 5089–5096.
(42) de Groot, M. T.; Koper, M. T. M., The influence of nitrate concentration and acidity on the electrocatalytic reduction of nitrate on platinum. *J. Electroanal. Chem.* **2004,** *562* (1), 81–94.
(43) Petrii, O. A.; Safonova, T. Y., Electroreduction of nitrate and nitrite anions on platinum metals: A model process for elucidating the nature of the passivation by hydrogen adsorption. *J. Electroanal. Chem.* **1992,** *331* (1), 897–912.
(44) Koper, M. T. M., Thermodynamic theory of multi-electron transfer reactions: Implications for electrocatalysis. *J. Electroanal. Chem.* **2011,** *660* (2), 254–260.
(45) Roling, L. T.; Herron, J. A.; Budiman, W.; Ferrin, P.; Mavrikakis, M., Dimethyl ether electro-oxidation on platinum surfaces. *Nano Energy* **2016,** *29*, 428–438.
(46) Akhade, S. A.; Bernstein, N. J.; Esopi, M. R.; Regula, M. J.; Janik, M. J., A simple method to approximate electrode potential-dependent activation energies using density functional theory. *Catal. Today* **2017,** *288*, 63–73.
(47) Xie, T.; Bodenschatz, C. J.; Getman, R. B., Insights into the roles of water on the aqueous phase reforming of glycerol. *React. Chem. Eng.* **2019,** *4* (2), 383–392.
(48) Bai, Y.; Mavrikakis, M., Mechanistic Study of Nitric Oxide Reduction by Hydrogen on Pt(100) (I): A DFT Analysis of the Reaction Network. *J. Phys. Chem. B* **2018,** *122* (2), 432–443.
(49) Hörold, S.; Vorlop, K.-D.; Tacke, T.; Sell, M., Development of catalysts for a selective nitrate and nitrite removal from drinking water. *Catal. Today* **1993,** *17* (1-2), 21–30.
(50) Shuai, D.; Choe, J. K.; Shapley, J. R.; Werth, C. J., Enhanced Activity and Selectivity of Carbon Nanofiber Supported Pd Catalysts for Nitrite Reduction. *Environ. Sci. Technol.* **2012,** *46* (5), 2847–2855.
(51) Toebes, M. L.; Van Dillen, J. A.; de Jong, K. P., Synthesis of supported palladium catalysts. *J. Mol. Catal. A Chem.* **2001,** *173* (1), 75–98.
(52) Paidar, M.; Roušar, I.; Bouzek, K., Electrochemical removal of nitrate ions in waste solutions after regeneration of ion exchange columns. *J. Appl. Electrochem.* **1999,** *29* (5), 611–617.
(53) Liu, Z.; Dong, S.; Zou, D.; Ding, J.; Yu, A.; Zhang, J.; Shan, C.; Gao, G.; Pan, B., Electrochemically mediated nitrate reduction on nanoconfined zerovalent iron: Properties and mechanism. *Water Res.* **2020,** *173*, 115596.
(54) Feedstock, E. W., Equipment design and cost estimation for small modular biomass systems, synthesis gas cleanup, and oxygen separation equipment. *Nat. Renew. Energy Lab.* **2006**.
(55) Van der Zwaan, B. C. C.; Schoots, K.; Rivera-Tinoco, R.; Verbong, G. P. J., The cost of pipelining climate change mitigation: An overview of the economics of $CH_4$, $CO_2$ and $H_2$ transportation. *Appl. Energy* **2011,** *88* (11), 3821–3831.
(56) Silverstein, C. G. a. J. Denitrification of high-nitrate, high-salinity wastewater. *Wat. Res.* **1999,** *33* (1), 223–229.
(57) Seidel, C., et al. "An assessment of the state of nitrate treatment alternatives." Final report of the american water works association, *Inorganic Contaminant Research & Inorganic Water Quality Joint Project Committees* **2011,** 118–121.
(58) Cammack, R.; Joannou, C.; Cui, X.-Y.; Martinez, C. T.; Maraj, S. R.; Hughes, M. N., Nitrite and nitrosyl compounds in food preservation. *Biochim. Biophys. Acta.* **1999,** *1411* (2-3), 475–488.
(59) Carocho, M.; Morales, P.; Ferreira, I. C., Natural food additives: Quo vadis? *Trends Food Sci.Technol.* **2015,** *45* (2), 284–295.
(60) Park, J.; Jin, K.; Sahasrabudhe, A.; Chiang, P.-H.; Maalouf, J. H.; Koehler, F.; Rosenfeld, D.; Rao, S.; Tanaka, T.; Khudiyev, T., In situ electrochemical generation of nitric oxide for neuronal modulation. *Nat. Nanotechnol.* **2020,** *15* (8), 690–697.
(61) Li, H.; Yan, C.; Guo, H.; Shin, K.; Humphrey, S. M.; Werth, C. J.; Henkelman, G., $Cu_xIr_{1-x}$ Nanoalloy Catalysts Achieve Near 100% Selectivity for Aqueous Nitrite Reduction to $NH_3$. *ACS Catal.* **2020,** *10* (14), 7915–7921.
(62) Clark, C. A.; Reddy, C. P.; Xu, H.; Heck, K. N.; Luo, G.; Senftle, T. P.; Wong, M. S., Mechanistic Insights into pH-controlled nitrite reduction to ammonia and hydrazine over rhodium. *ACS Catal.* **2019,** *10* (1), 494–509.
(63) Feng, Y.; Yang, H.; Zhang, Y.; Huang, X.; Li, L.; Cheng, T.; Shao, Q., Te-Doped Pd Nanocrystal for Electrochemical Urea Production by Efficiently Coupling Carbon Dioxide Reduction with Nitrite Reduction. *Nano Lett.* **2020,** *20* (11), 8282–8289.

**Table of contents:**

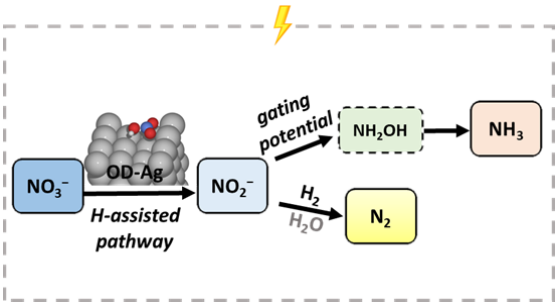


**Table of contents text:**

**Strong preference for electrocatalytic nitrate-to-nitrite reduction on Ag enables an innovative strategy of denitrifying wastewater with desirable ultrahigh selectivity.**